Energy Advances

ROYAL SOCIETY OF CHEMISTRY

COMMUNICATION

View Article Online
View Journal | View Issue

Check for updates

Cite this: *Energy Adv.*, 2024, 3, 2903

Received 19th September 2024,
Accepted 7th November 2024

DOI: 10.1039/d4ya00539b

rsc.li/energy-advances

Room-temperature, one-step synthesis of Mn_3O_4 nanoparticles using morpholine as a complexing and precipitating agent: toward a cathode material for zinc-ion batteries†

Saad G. Mohamed, *[ab] Jixu Wan[c] and Xuejin Li*[c]

The quest for sustainable energy storage has spotlighted zinc-ion batteries (ZIBs) for their safety, cost-effectiveness, and eco-friendliness. Manganese oxides, particularly Mn_3O_4, stand out as promising cathode materials due to their electrochemical virtues and affordability. However, traditional synthesis methods like solid-state reactions, hydrothermal processes, and sol–gel techniques often entail complex procedures, high temperatures, and environmentally harmful chemicals, which impede their practical applications. This study introduces a novel, eco-friendly synthesis route for Mn_3O_4 nanoparticles *via* the room-temperature reaction of morpholine with manganese nitrate for 24 h, reducing both the environmental impact and the complexity of production. This method yields Mn_3O_4 nanoparticles with enhanced crystallinity and surface area, which is crucial for improved electrochemical performance in ZIBs by offering increased active sites for zinc intercalation. The resultant high-performance Mn_3O_4 nanoparticles align with sustainable practices and hold the potential for advancing next-generation energy storage technologies. The detailed structure and electrochemical performance were investigated in detail in this study. The produced Zn//Mn_3O_4 nanoparticles cell exhibited a remarkable electrochemical performance, which displayed a high reversible capacity of 209.7 mAh g^{-1} after 300 cycles at 0.6 A g^{-1}.

Introduction

The growing demand for energy storage solutions has driven extensive research into developing advanced materials for batteries.[1,2] Among the various types of batteries, zinc-ion batteries (ZIBs) have garnered significant attention due to their safety, cost-effectiveness, and environmental friendliness.[3] However, the performance of ZIBs is heavily dependent on the properties of the electrode materials used.[4] In this context, the synthesis of high-surface-area materials with superior electrochemical properties is crucial.[5]

Manganese oxides, particularly Mn_3O_4, have been extensively studied as cathode materials for energy storage applications due to their abundance, low cost, and favorable electrochemical properties.[6–8] Mn_3O_4 has emerged as a promising candidate for use in aqueous ZIBs owing to its ability to provide a balance between both considerable capacity and high voltage.[9,10] However, like other manganese-based oxides, Mn_3O_4 suffers from capacity degradation and suboptimal rate performance, primarily attributed to its inherent poor conductivity and the dissolution of Mn^{2+} ions.[11] Traditionally, Mn_3O_4 has been synthesized through various techniques such as solid-state reactions,[12] hydrothermal processes,[13] and sol–gel methods,[14] each requiring multiple steps, high temperatures, or the use of hazardous chemicals.

The solid-state reaction method, while effective in producing Mn_3O_4, often involves prolonged heating at high temperatures, leading to large particle sizes and reduced surface area, which can negatively impact the material's electrochemical performance. Hydrothermal and sol–gel methods, on the other hand, typically require the use of surfactants or organic solvents to control the morphology and particle size of Mn_3O_4, introducing additional steps and potential environmental concerns. Although successful in producing Mn_3O_4, these conventional methods often involve complex synthesis procedures and non-eco-friendly reagents, which can limit their scalability and sustainability.

In this study, we explore a novel and green synthesis route for Mn_3O_4 using the reaction of morpholine with manganese nitrate at room temperature. This method significantly reduces the number of synthesis steps and avoids the use of high temperatures or hazardous chemicals, making it an environmentally friendly alternative to conventional techniques. Morpholine, acting as both a complexing agent and a base, facilitates the controlled precipitation of manganese hydroxide, which is then

[a] *Mining and Metallurgy Engineering Department, Tabbin Institute for Metallurgical Studies (TIMS), Tabbin, Helwan 109, Cairo 11421, Egypt. E-mail: saadmohamed@tims.gov.eg*
[b] *Academy of Scientific Research & Technology (ASRT), 101 Kasr Al-Ainy St., Cairo, Egypt*
[c] *School of Materials Science and Engineering, State Key Laboratory of Heavy Oil Processing, China University of Petroleum (East China), Qingdao, 266580, P. R. China. E-mail: lxjupc@gmail.com*

† Electronic supplementary information (ESI) available. See DOI: https://doi.org/10.1039/d4ya00539b

oxidized to Mn_3O_4 in a single step under mild conditions. This synthesis approach not only simplifies the production process but also yields Mn_3O_4 with a high crystallinity and surface area, which is critical for enhancing the electrochemical performance of ZIBs by providing more active sites for Zn^{2+} intercalation. Moreover, using this green synthesis method aligns with sustainable chemistry principles, offering a more straightforward and eco-friendly approach to producing high-performance Mn_3O_4. The resultant Mn_3O_4 exhibits high performance in ZIBs, making it an attractive material for next-generation energy storage devices. By reducing the complexity and environmental impact of the synthesis process, this study contributes to the advancement of sustainable materials for energy applications.

Experimental procedures

The experimental procedures are presented in the ESI.†

Results and discussion

The crystalline nature and phase of the as-prepared Mn_3O_4 nanoparticles were investigated using X-ray diffraction (XRD). Fig. 1a's XRD pattern reflects the hausmannite Mn_3O_4 tetragonal phase (JCPDS card no. 01-089-4837), showing the effective synthesis of high crystalline Mn_3O_4.

The as-prepared Mn_3O_4 nanoparticles exhibit strong diffraction peaks at 2θ degrees (with the corresponding lattice planes) of 17.99 (101), 28.96 (112), 31.00 (200), 32.32 (103), 36.04 (211), 38.08 (004), 44.53 (220), 49.91 (204), 50.76 (105), 53.96 (312), 56.12 (303), 58.62 (321), 59.86 (224), 63.17 (116), 64.62 (400), 67.64 (411), 69.71 (305), 74.21 (413), 76.73 (422), and 77.64 (422). No further crystalline phases were found, and the significant diffraction peaks in patterns detected by XRD show that the resultant product is highly crystallized.

Furthermore, the Raman spectrum distinctly exhibits the characteristic signatures of crystalline Mn_3O_4. Notably, three pronounced vibrational peaks are observed (Fig. 1c) at 316, 370, and 663 cm^{-1}, corresponding to the E_g, T_{2g}, and A_{1g} active modes of Mn_3O_4, respectively. The most intense peak is attributed to the Mn–O stretching vibration of tetrahedral Mn^{2+} within the spinel Mn_3O_4 structure. The two less intense peaks are associated with the combined vibrational modes of oxygen atoms in both tetrahedral and octahedral sites.[15–17] The X-ray photoelectron spectroscopy (XPS) analysis of the Mn 2p region

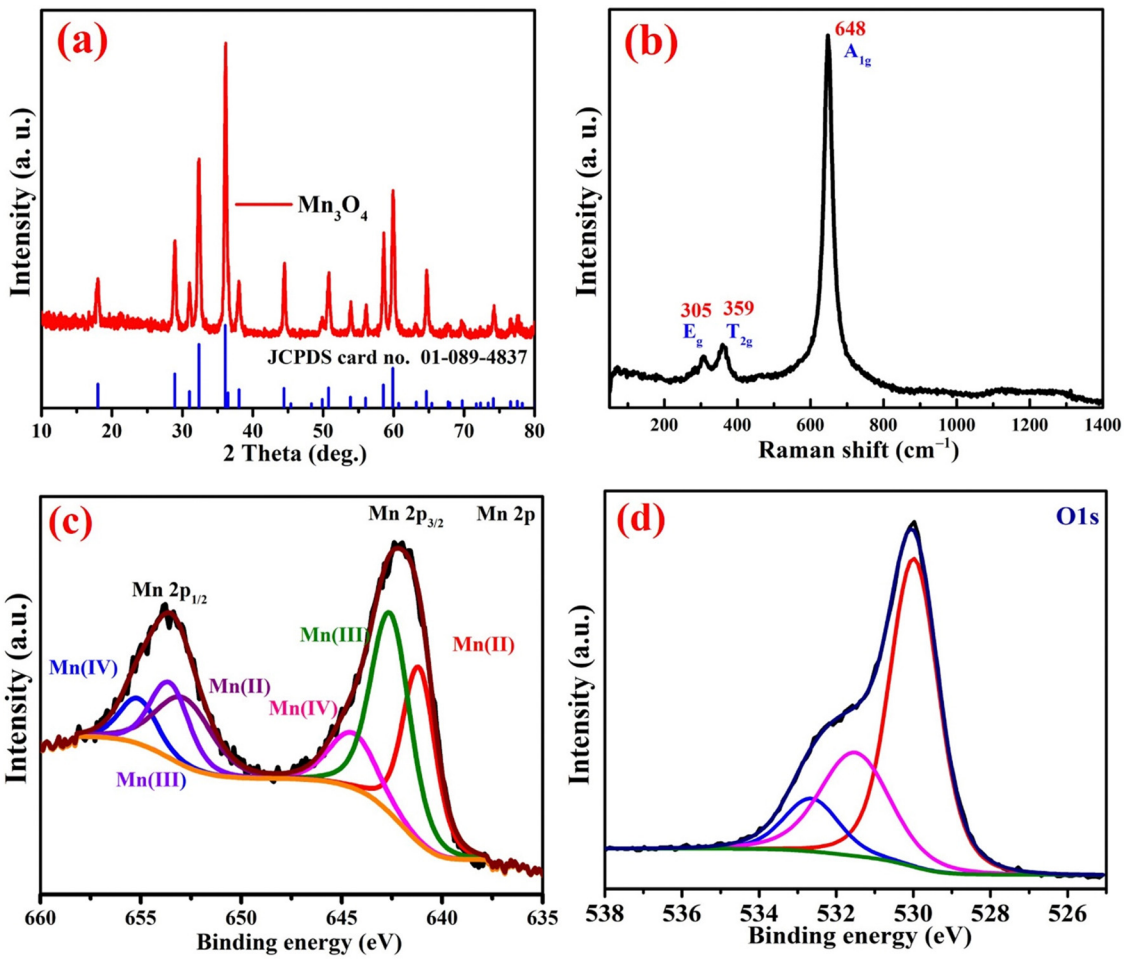

Fig. 1 (a) XRD pattern, (b) Raman spectrum, (c) Mn 2p XPS high-resolution spectrum, and (d) O 1s XPS high-resolution spectrum of the produced Mn_3O_4 nanoparticles.

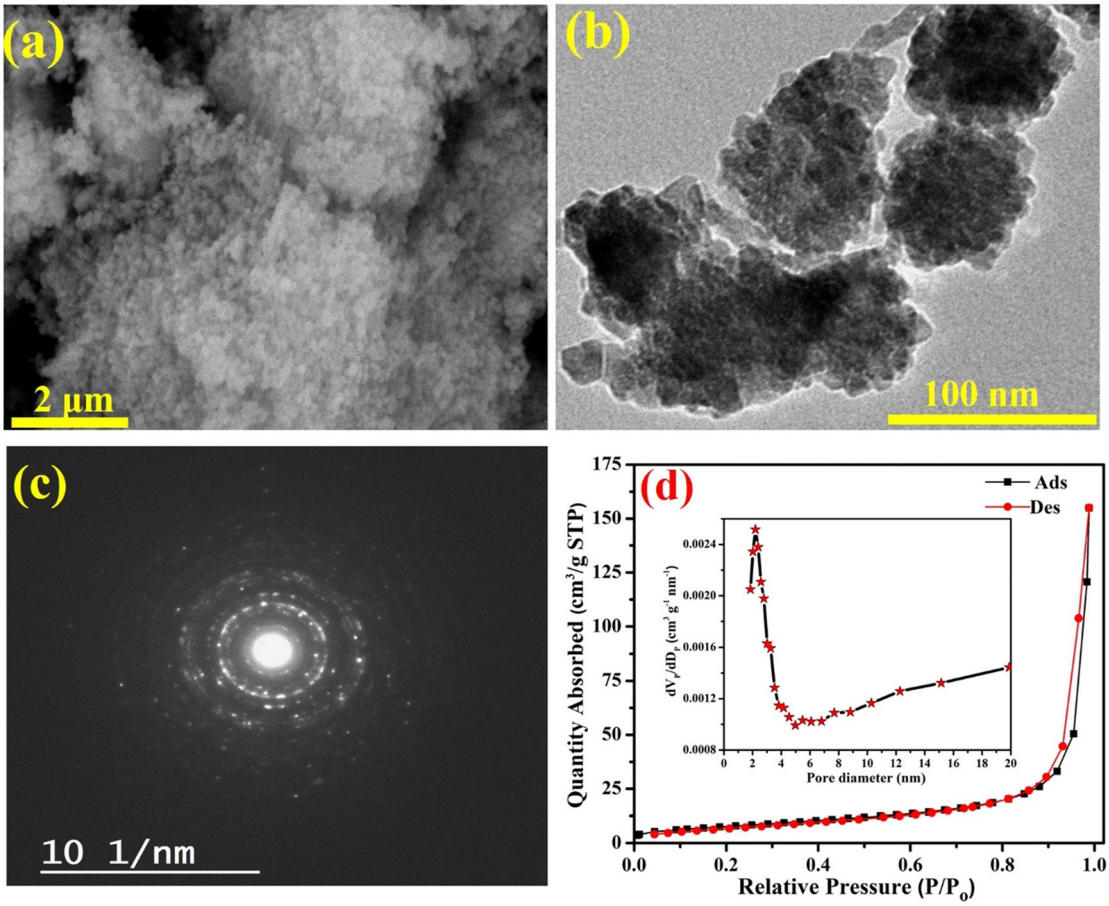

Fig. 2 (a) SEM image, (b) TEM Image, (c) SAED, and (d) Nitrogen adsorption and desorption isotherm (inset shows the pore distribution) of the produced Mn_3O_4 nanoparticles.

for Mn_3O_4 nanoparticles reveals a complex valence (mixed valence) state for manganese, as depicted in Fig. 2c. The binding energy peaks at 642.18 eV and 653.68 eV correspond to Mn $2p_{3/2}$ and Mn $2p_{1/2}$, respectively. The spectral peaks can be deconvoluted to features at 641.18 eV and 652.9 eV, which are attributable to Mn^{2+}, while those at 642.68 eV and 653.68 eV align with Mn^{3+}, and the peaks at 644.48 eV and 655.28 eV are indicative of Mn^{4+}.[18] The occurrence of Mn^{4+} may also suggest surface oxidation processes, potentially converting Mn^{2+} to Mn^{3+} within Mn_3O_4.[18,19] Fig. 2d presents the deconvoluted O 1s XPS spectrum for Mn_3O_4 nanoparticles synthesized *via* a green method. Three distinct binding energies are identified: 529.9 eV, 531.6 eV, and 532.7 eV. These are respectively attributed to the Mn–O–Mn linkages in the tetravalent oxide, oxygen defects and/or Mn–OH bonds, and H–O–H of adsorbed water molecules.[17,19,20]

The MnO_3O_4 formation mechanism can be described as follows: the reaction of morpholine ($O(CH_2CH_2)_2NH$) with manganese nitrate ($Mn(NO_3)_2$) aqueous solution at room temperature can be stepwise ascribed by the following steps: 1-dissolution of $Mn(NO_3)_2$ in water forms Mn^{2+} and NO^{3-} ions. 2-Morpholine acts as a multifunctional agent, serving as both a complexing agent and a base. 3-$Mn(OH)_2$ and $Mn(OH)_3$ form due to an increase in pH from morpholine, which can further dehydrate and oxidize to form Mn_3O_4. The following equation describes the possible mechanism of the reaction between manganese nitrate and morpholine in an aqueous solution.

$$Mn(NO_3)_2 \rightarrow Mn^{2+} + 2NO_3^-$$

$$Mn^{2+} + O(CH_2CH_2)_2NH \rightarrow [Mn(O(CH_2CH_2)_2NH)]^{2+}$$

$$O(CH_2CH_2)_2NH + H_2O \rightarrow O(CH_2CH_2)_2NH^{2+} + OH^-$$

$$Mn^{2+} + 2OH^- \rightarrow Mn(OH)_2\downarrow$$

$$Mn^{2+} + NO_3^- + H_2O \rightarrow Mn^{3+} + NO_2^- + 2OH^-$$

$$Mn^{3+} + 3OH^- \rightarrow Mn(OH)_3\downarrow$$

$$2Mn(OH)_3 + Mn(OH)_2 + NO_3^- \rightarrow Mn_3O_4 + NO_2^- + 3H_2O + 2OH^-$$

The following equation can describe the overall reaction;

$$3Mn(NO_3)_2 + 4O(CH_2CH_2)_2NH + 2H_2O \rightarrow Mn_3O_4 + 4O(CH_2CH_2)_2NH^{2+} + 6NO_2^- + 4OH^-$$

The morphological characteristics of the synthesized Mn_3O_4 nanoparticles were thoroughly examined through scanning electron microscopy (SEM). As represented in Fig. 2a, the Mn_3O_4 nanoparticles are composed of uniformly distributed micron-sized aggregates, with individual particle sizes ranging from approximately 10 to 60 nm with porous features, as illustrated in transmission electron microscope image (TEM), Fig. 2b. The nanoparticles exhibit an irregular morphology, which is indicative of a potentially large specific surface area. This structural feature is anticipated to contribute favorably to their electrochemical performance. The high degree of crystallinity (polycrystalline nature) is clearly evidenced by the well-defined SAED pattern shown in Fig. 2c. The structure is expected to offer an ample contact area for electrolyte permeation while also providing a sufficient number of active sites to facilitate the insertion and extraction of Zn^{2+} ions. In Fig. 2d, the N_2 adsorption/desorption isotherms and the corresponding pore size distributions (shown in the inset) are presented. The isotherms exhibit characteristics typical of type IV, which are commonly associated with the mesoporous nature of Mn_3O_4 nanoparticles. Notably, the surface area of the Mn_3O_4 nanoparticles was measured to be 28.8 $m^2\ g^{-1}$. The analysis of pore size distributions reveals that a significant portion of the pores in the Mn_3O_4 nanoparticles fall within the mesoporous range. This finding suggests that the produced Mn_3O_4 nanoparticles contain a considerable number of pores with diameters consistent with mesoporous structures.

Cyclic voltammetry (CV) and galvanostatic charge–discharge (GCD) tests were performed to evaluate the electrochemical behavior and performance of Mn_3O_4 nanoparticles. Fig. 3a presents the first six CV curves of Mn_3O_4 nanoparticles electrode at a scan rate of 0.1 mV s^{-1}, where two distinct pairs of redox peaks are observed at 1.25/1.38 V (cathodic scan) and 1.56/1.60 V (anodic scan). During the discharge process, the reduction peaks at 1.38 V and 1.25 V correspond to the insertion of H^+ and Zn^{2+} ions, respectively, along with the reduction of Mn^{3+} to Mn^{2+} and Mn^{4+} to Mn^{3+}.[18,19,21] In the charging process, the oxidation peaks at 1.56 V and 1.60 V are associated with the extraction of Zn^{2+} and H^+ ions,[22] accompanied by the oxidation of Mn^{2+} or Mn^{3+} to Mn^{3+} or Mn^{4+}.[18,19] The increasing peak current intensity by the cycling could be that during the initial charge process, the Mn_3O_4 phase transforms into an intermediate Mn_5O_8 phase. Subsequently, as Mn^{2+} ions dissolve, the Mn_5O_8 phase gradually converts into spinel-layered MnO_2. Also, as Mn_5O_8 transitions into MnO_2, the intensity of the reduction peaks progressively increases.[23]

As illustrated in Fig. 3b, during the initial charge–discharge cycles at a current density of 0.2 A g^{-1}, the Mn_3O_4 nanoparticles electrode demonstrated a progressive increase in capacity. Notably, the charge/discharge capacity started at 94.0/75.7 and reached the high value of 778.7/767.4 mAh g^{-1} at cycle number 37. This phenomenon can be attributed to the typical

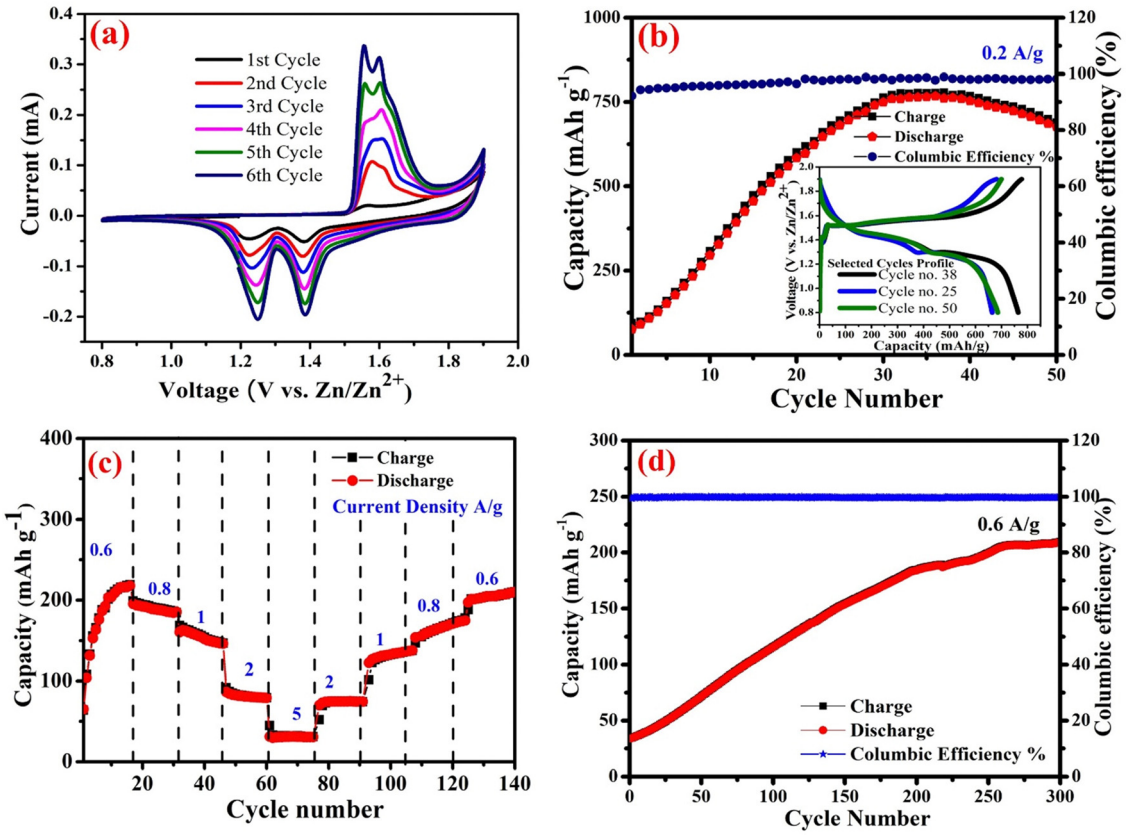

Fig. 3 Electrochemical performances of the Mn_3O_4 nanoparticles cathode: (a) CV curves at a scan rate of 0.1 mV s^{-1}, (b) cycle performance at 0.2 A g^{-1} and inset is discharge/charge profiles of selected cycles, (c) rate property, and (d) cycling performance at 0.6 A g^{-1}.

activation process observed in manganese-based cathodes when operating in an aqueous electrolyte.[22,24] After cycle 40, fluctuations in the capacity trend were observed. The electrode maintained a reversible capacity of 689.3 mAh g^{-1} by continuous cycling, which can be attained in the 50th cycle. The coulombic efficiency (CE) remained consistently around 99% throughout the multiple cycles.

Fig. 3b′ inset depicts the Mn_3O_4 nanoparticles cathode charge–discharge profile based on the selected cycles in Fig. 3b. Remarkably, the discharge profile displays two distinct plateaus at 1.25 to 1.3 V and 1.4 to 1.5 V, corresponding to the insertion of H^+ and Zn^{2+} ions into the Mn_3O_4 matrix. The plateaus observed at approximately 1.55 V and 1.65 V in the charge profiles are associated with extracting H^+ and Zn^{2+} ions from the Mn_3O_4 hosts. These findings agree with the two pairs of redox peaks observed in the CVs. Similar behavior has been reported in Mn_3O_4 electrodes as ZIB cathode.[25,26]

As illustrated in Fig. 3c, the rate-capacity results demonstrate a gradual decline in reversible capacity with increasing current densities. At a current density of 0.6 A g^{-1}, the charge/discharge capacity progressively increases after 15 cycles to 219/217.8 mAh g^{-1}. The Mn_3O_4 nanoparticles electrode delivered charge/discharge capacities of 186.3/184.3, 146.8/146.2, 79.3/79.1, and 30.9/30.5 mAh g^{-1} at current densities of 0.8, 1, 2, and 5 A g^{-1}, respectively. However, when the current density is reduced again in the same trend from 5 A g^{-1} to 0.6 A g^{-1}, the reversible capacity is restored to 74.3/74.5, 147.0/154.0, 187.6/194.6, and 212.7/211.1 mAh g^{-1}, as the current density reversed to 2, 1, 0.8, and 0.6 mA g^{-1}, respectively, exhibiting superior rate performance, which could be ascribed to the large specific surface area and the porous feature of the Mn_3O_4 which facilitates the efficient insertion and extraction of Zn^{2+} ions during the discharge–charge processes, further contributing to its improved electrochemical performance.

Moreover, Fig. 3d demonstrates the long-term cycling stability at a current density of 0.6 A g^{-1}. It is observed that the specific capacity gradually increases with the progression of cycling, which is attributable to the material activation. This activation arises primarily from two factors: (1) the infiltration of the electrolyte into the cathode enhances the reversible reactions and minimizes the electrochemical inactivity of the active materials, and (2) the synergistic interaction between Zn^{2+} and Mn^{2+}, coupled with the redox reaction of Mn^{2+}, necessitates time for diffusion from the electrolyte into the bulk phase of the positive material.[18,27] The capacity of the electrode demonstrates a gradual increase throughout the cycling process, culminating in a higher charge/discharge capacity of 209.7/209.1 mAh g^{-1} after 300 cycles.

To gain a more comprehensive understanding of the dynamic mechanisms involved in Zn//Mn_3O_4 cell during charge storage, cyclic voltammetry (CV) was conducted at varying scan rates. As observed in Fig. 4a, an increase in scan rate results in a shift of the reduction peaks toward lower potentials and the oxidation peaks toward higher potentials, indicative of enhanced polarization. Additionally, the current intensity of peak 2 and peak 3 becomes significantly more noticeable, which can be attributed to the fact that with increasing current, the reaction process becomes progressively dominated by H^+ insertion.[19] The relationship between the current (i) and scan rate (v) can be expressed using the equation $i = av^b$, where b values of 0.5 and 1.0 correspond to diffusion-controlled and pseudocapacitance-controlled reactions, respectively.[28,29] The calculated b values for peaks 1, 2, and 3 of Zn//Mn_3O_4-nanoparticles cell, as determined from the correlation between $\log(i)$ and $\log(v)$ (Fig. 4b), are 0.885, 0.796, and 0.976, respectively. The raised b values observed for the Mn_3O_4 nanoparticles electrode suggest pronounced pseudocapacitive properties similar to those found in the previous related Mn_3O_4-base electrodes,[18,19] which indicates a substantial rate performance.

Additionally, the contributions from capacitive and diffusion processes can be differentiated into capacitive-controlled (k_1v) and diffusion-controlled ($k_2v^{1/2}$) components, as expressed in the equation: $i(V) = k_1v + k_2v^{1/2}$, which can be reformulated as $i(V)/v^{1/2} = k_1v^{1/2} + k_2$.[30] The constants k_1 and k_2 can be determined by plotting the relationship between $i(V)/v^{1/2}$ and $v^{1/2}$, corresponding to the capacitive behavior and diffusion-controlled process.

Fig. 4c illustrates the pseudocapacitance contributions of Zn//Mn_3O_4-nanoparticles cell with scan rates, recording values of 60.4%, 72.6%, 77.4%, 80.2%, and 82.9% at scan rates of 0.1, 0.3, 0.5, 0.7, and 1 mV s^{-1}, respectively. For instance, the CV profile for the capacitive contribution compared with that of the diffusion-controlled current at 0.1 mV s^{-1} is around 60.4% capacitive-dominated to 39.6% diffusion-controlled process, as shown in Fig. 4d.

The capacitance characteristics of the electrode exhibit a pronounced increase with rising scan rates, enhancing its capacity to store and release charges at elevated currents. This improvement bestows upon the Zn//Mn_3O_4-nanoparticles cell superior and preeminent ZIB performance.

Even at a low temperature of −10 °C, the Zn//Mn_3O_4-nanoparticle cell in a $ZnSO_4$-0.1 M $MnSO_4$-30% 1,2-dimethoxyethane (DME) electrolyte demonstrates a reversible capacity of 50 mAh g^{-1} with nearly 100% CE after 1500 cycles at a current density of 0.2 A g^{-1} (Fig. 4d), with charge/discharge profile, shown in Fig. 4d′ inset, is similar to the room temperature profile without DME addition, indicating excellent compatibility at low temperatures. It is noted that the activation process takes longer cycles, which can be attributed to the decrease in the migration rate of ions in the electrolyte, resulting in a substantial reduction in ionic conductivity. This, in turn, directly increases the battery's internal resistance, adversely impacting its charging and discharging performance.[31]

Conclusions

This study successfully demonstrates a green and efficient synthesis route for Mn_3O_4 using morpholine and manganese nitrate at room temperature. The resulting Mn_3O_4 nanoparticles exhibit superior crystallinity and high surface area, significantly enhancing its electrochemical performance in ZIBs. By simplifying the synthesis process and eliminating the need for high temperatures and toxic chemicals, this method not only adheres to sustainable chemistry principles

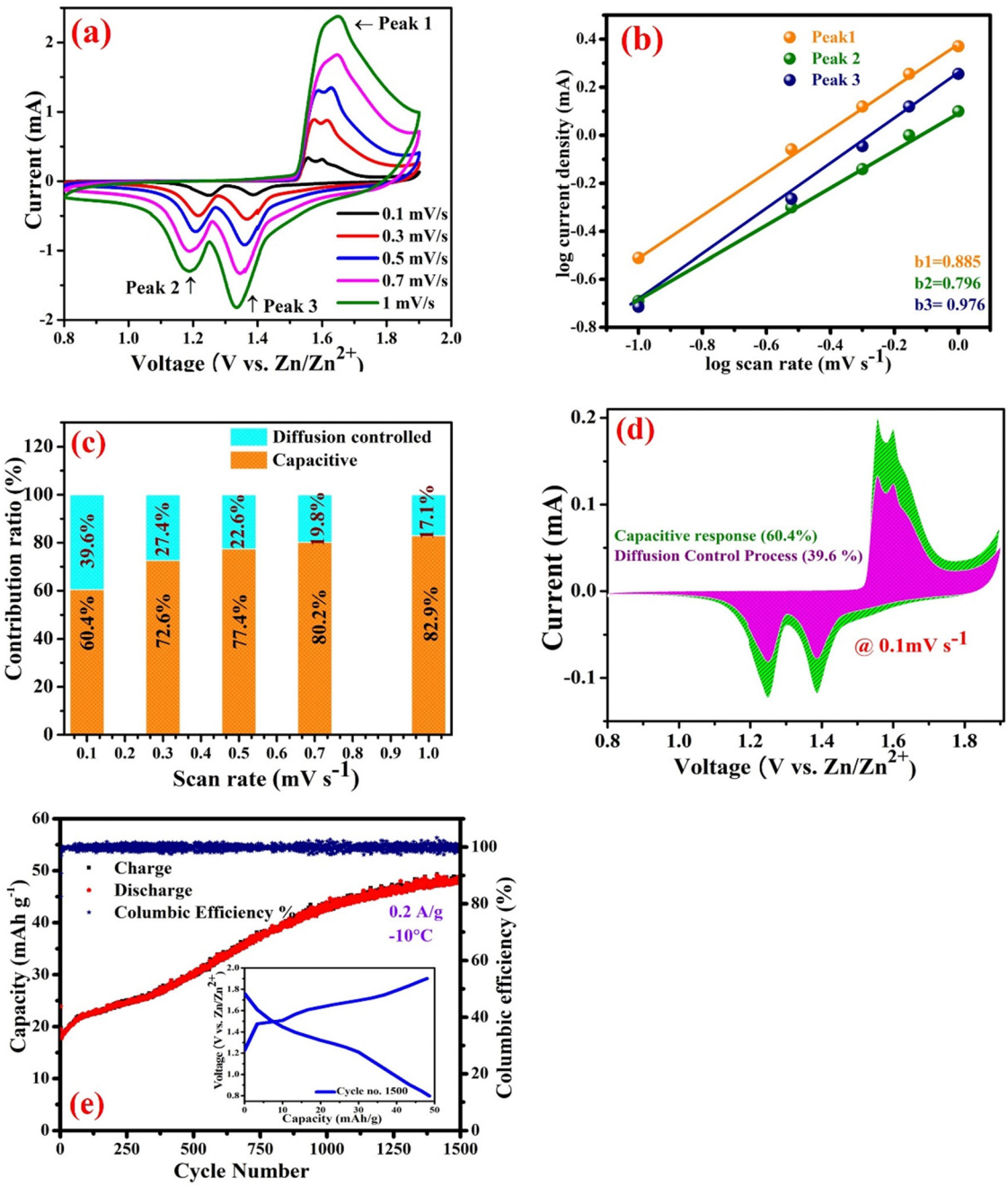

Fig. 4 (a) CV curves of Mn_3O_4 nanoparticles cathode at different scan rates, (b) log *i* and log *v* plots resulted from Fig. 4a, (c) the capacitive/diffusion contribution ratios in Mn_3O_4 nanoparticles cathode electrode, (d) capacitive contribution to the total capacity at a scan rate of 0.1 mV s^{-1}, and (e) cycling performance operated at −10 °C at 0.2 A g^{-1} and inset is discharge/charge profiles of the cycle number 1500.

but also overcomes traditional synthesis techniques' limitations. The high performance of the synthesized Mn_3O_4 nanoparticles in ZIBs underscores its potential as a viable material for future energy storage solutions. This work contributes to the ongoing efforts to develop eco-friendly and cost-effective energy storage technologies, marking a significant step toward the practical application of high performance. This study also opens the gates for preparing Mn_3O_4 derivatives using the same protocol.

Data availability

The current study's data are available from the corresponding author upon request.

Conflicts of interest

There are no conflicts to declare.

Acknowledgements

The authors express their gratitude to the Academy of Scientific Research & Technology (ASRT, Egypt) for supporting the STARS-ASRT fellowship, the Tabbin Institute for Metallurgical Studies, and China University of Petroleum (East China) for providing the necessary facilities to conduct the study.

References

1 G. G. Njema, R. B. O. Ouma and J. K. Kibet, *J. Renewable Energy*, 2024, **2024**, 2329261.
2 S. Nyamathulla and C. Dhanamjayulu, *J. Energy Storage*, 2024, **86**, 111179.
3 L. Li, S. Jia, Y. Shi, C. Wang, H. Qiu, Y. Ji, M. Cao and D. Zhang, *Inorg. Chem. Front.*, 2024, **11**, 4485–4498.
4 C. Qiu, H. Huang, M. Yang, L. Xue, X. Zhu, Y. Zhao, M. Ni, T. Chen and H. Xia, *Energy Storage Mater.*, 2024, 103736, DOI: **10.1016/j.ensm.2024.103736**.
5 Y. Liu and X. Wu, *J. Energy Chem.*, 2021, **56**, 223–237.
6 Y. Zhao, Y. Zhu and X. Zhang, *InfoMat*, 2020, **2**, 237–260.
7 X. Ke, L. Li, S. Wang, A. Wang, Z. Jiang, F. R. Wang, C. Kuai and Y. Guo, *Next Energy*, 2024, **2**, 100095.
8 S. K. Abdel-Aal, S. Y. Attia and S. G. Mohamed, *J. Electron. Mater.*, 2019, **48**, 4977–4986.
9 L. Wang, X. Cao, L. Xu, J. Chen and J. Zheng, *ACS Sustainable Chem. Eng.*, 2018, **6**, 16055–16063.
10 T.-B. Song, Z.-H. Huang, X.-Q. Niu, X.-R. Zhang, J.-S. Wei and H.-M. Xiong, *ChemSusChem*, 2022, **15**, e202102390.
11 B. Zhang, P. Dong, S. Yuan, Y. Zhang, Y. Zhang and Y. Wang, *Chem Bio Eng.*, 2024, **1**, 113–132.
12 W. Z. Wang, C. K. Xu, G. H. Wang, Y. K. Liu and C. L. Zheng, *Adv. Mater.*, 2002, **14**, 837–840.
13 H. Dhaouadi, A. Madani and F. Touati, *Mater. Lett.*, 2010, **64**, 2395–2398.
14 A. K. M. A. Ullah, A. K. M. F. Kibria, M. Akter, M. N. I. Khan, M. A. Maksud, R. A. Jahan and S. H. Firoz, *J. Saudi Chem. Soc.*, 2017, **21**, 830–836.
15 A. Pramanik, S. Maiti, M. Sreemany and S. Mahanty, *ChemistrySelect*, 2017, **2**, 7854–7864.
16 D. Lan, M. Qin, R. Yang, H. Wu, Z. Jia, K. Kou, G. Wu, Y. Fan, Q. Fu and F. Zhang, *J. Mater. Sci.: Mater. Electron.*, 2019, **30**, 8771–8776.
17 J. K. Sharma, P. Srivastava, S. Ameen, M. S. Akhtar, G. Singh and S. Yadava, *J. Colloid Interface Sci.*, 2016, **472**, 220–228.
18 C. Yin, J. Chen, C.-L. Pan, Y. Pan and J. Hu, *ACS Appl. Energy Mater.*, 2022, **5**, 14144–14154.
19 Y.-F. Guo, Z.-H. Luo, N. Zhang, P.-F. Wang, Z.-L. Liu, Q.-Z. Lai, J. Shu and T.-F. Yi, *J. Colloid Interface Sci.*, 2025, **677**, 459–469.
20 Q.-L. Gao, D.-S. Li, X.-M. Liu, Y.-F. Wang, W.-L. Liu, M.-M. Ren, F.-G. Kong, S.-J. Wang and R.-C. Zhou, *Electrochim. Acta*, 2020, **335**, 135642.
21 T. Xiong, Z. G. Yu, H. Wu, Y. Du, Q. Xie, J. Chen, Y.-W. Zhang, S. J. Pennycook, W. S. V. Lee and J. Xue, *Adv. Eng. Mater.*, 2019, **9**, 1803815.
22 Y. He, Y. Pu, B. Zhu, H. Zhu, C. Wang, W. Tang and H. Tang, *J. Alloys Compd.*, 2023, **934**, 167933.
23 H. Chen, W. Zhou, D. Zhu, Z. Liu, Z. Feng, J. Li and Y. Chen, *J. Alloys Compd.*, 2020, **813**, 151812.
24 V. Soundharrajan, B. Sambandam, S. Kim, S. Islam, J. Jo, S. Kim, V. Mathew, Y.-K. Sun and J. Kim, *Energy Storage Mater.*, 2020, **28**, 407–417.
25 M. Sun, D.-S. Li, Y.-F. Wang, W.-L. Liu, M.-M. Ren, F.-G. Kong, S.-J. Wang, Y.-Z. Guo and Y.-M. Liu, *ChemElectroChem*, 2019, **6**, 2510–2516.
26 J. Hao, J. Mou, J. Zhang, L. Dong, W. Liu, C. Xu and F. Kang, *Electrochim. Acta*, 2018, **259**, 170–178.
27 N. Liu, X. Wu, Y. Yin, A. Chen, C. Zhao, Z. Guo, L. Fan and N. Zhang, *ACS Appl. Mater. Interfaces*, 2020, **12**, 28199–28205.
28 R. E. Mostafa, S. S. Mahmoud, N. S. Tantawy and S. G. Mohamed, *ChemNanoMat*, 2024, **10**, e202300610.
29 K. Ma, S. Ge, R. Fu, C. Feng, H. Zhao, X. Shen, G. Liang, Y. Zhao and Q. Jiao, *Chem. Eng. J.*, 2024, **484**, 149525.
30 J. Wang, J. Polleux, J. Lim and B. Dunn, *J. Phys. Chem. C*, 2007, **111**, 14925–14931.
31 L. F. Xiao, Y. L. Cao, X. P. Ai and H. X. Yang, *Electrochim. Acta*, 2004, **49**, 4857–4863.